Title
Microstructural tunability of co-continuous bijel-derived electrodes to provide high energy and power densities

Journal
Journal of Materials Chemistry A, 4(3)

ISSN
2050-7488

Authors
Witt, JA
Mumm, DR
Mohraz, A

Publication Date
2016

DOI
10.1039/c5ta06260h

Peer reviewed

Journal of Materials Chemistry A

PAPER

Cite this: J. Mater. Chem. A, 2016, 4, 1000

Microstructural tunability of co-continuous bijel-derived electrodes to provide high energy and power densities†

J. A. Witt, D. R. Mumm and A. Mohraz*

Emerging demands for national security, transportation, distributed power, and portable systems call for energy storage and conversion technologies that can simultaneously deliver large power and energy densities. To this end, here we report three-dimensional Ni/Ni(OH)$_2$ composite electrodes derived from a new class of multi-phase soft materials with uniform, co-continuous, and tunable internal microdomains. These remarkable morphological attributes combined with our facile chemical processing techniques allow the electrode's salient morphological parameters to be independently tuned for rapid ion transport and a large volumetric energy storage capacity. Through microstructural design and optimization, our composite electrodes can simultaneously deliver energy densities equal to that of batteries and power densities equivalent to or greater than that of the best supercapacitors, bridging the gap between these modern technologies. Our synthesis procedure is robust and can be extended to a myriad of other chemistries for next generation energy storage materials.

Received 10th August 2015
Accepted 30th November 2015

DOI: 10.1039/c5ta06260h

www.rsc.org/MaterialsA

Introduction

Electrochemical supercapacitors and rechargeable batteries have emerged as promising technologies for advanced energy storage and conversion, but their uses are currently limited by the energy and power densities that they can deliver.[1,2] Supercapacitors characteristically enjoy high charge/discharge rates and extensive cycle life but suffer from low energy densities, restraining their use to high-power, short duration applications.[3,4] By contrast, batteries can deliver energy for longer periods but only at reduced rates, making them suitable for low-power applications that demand extended use between charge cycles. The performance of electrodes in batteries and supercapacitors is governed by their chemical makeup and microstructural configuration at the length scales that govern energy storage and charge transport in electrochemical composites.[5] Microstructurally, the envisioned ideal configuration is one that simultaneously provides percolating passages for electrons and ions to freely flow throughout the structure, minimizes the length and resistance of transport pathways, and enables a large volumetric density of electrolytically active materials. In addition, the method of fabrication must be scalable to allow for large amounts of total stored energy.[6,7] There have been many preliminary attempts to create such a network using foams,[8] nanocolumns,[9] nanowires,[10] nanoflakes,[11] and lithographically defined microstructures.[12] Nonetheless, these designs have not been able to meet the requirements of next generation electrodes mentioned above. For example, foam-based structures benefit from simple and scalable fabrication techniques but the characteristic pore size in these systems (typically hundreds of microns and larger) is at least an order of magnitude larger than what is needed (tens of microns or smaller) to optimize the charge transport pathways and maximize the volume fraction of active materials. Conversely, lithography-based systems enjoy detailed microstructural prescription and optimization by design, but lack the required scalability for production in macroscopic dimensions. Recently, Zhang *et al.* have shown that inverse opal structures consisting of conductive metal backbones and electrolytically active phases can offer rapid charge and discharge rates while maintaining a fairly modest energy density.[13,14] However, the particular pore configuration of an inverse opal (spherical pockets connected by small interstitial windows) does not lend itself to the level of morphological control needed to independently tune the electrode's capacity and power density while also conserving the required co-continuity to avoid current constriction in the charge carrier transport pathways. The fabrication technique also limits the height of the electrode to ~15 μm, restricting the total amount of stored energy in these systems.[14]

Further advances toward the ideal electrode morphology can only be achieved through co-continuous microstructured composites with highly controllable and uniform internal domains. Such characteristics are uniquely met in a new class of soft materials known as bicontinuous interfacially jammed emulsion gels (bijels).[15] Bijels are formed through arrested

Department of Chemical Engineering & Materials Science, University of California, Irvine, CA 92697, USA. E-mail: mohraz@uci.edu

† Electronic supplementary information (ESI) available. See DOI: 10.1039/c5ta06260h

spinodal decomposition of a binary liquid mixture by neutrally wetting colloidal particles.[16] During phase separation, the particles sequester to the fluid–fluid interface and become jammed once the interfacial area is sufficiently reduced to just accommodate them. The resulting non-equilibrium material consists of two uniform, interpenetrating and continuous fluid domains separated by a colloid monolayer. Importantly, the characteristic domain size in these dynamically self-similar systems, herein denoted as ξ (see Fig. 2 for definition), is directly related to the internal surface area per unit volume, S_v, and can be tuned through the colloid volume fraction and wetting properties.[17] Through post-processing techniques recently pioneered in our laboratory, these soft materials can be converted into macroporous and hierarchically porous metals, ceramics, and polymers with tunable pore size distributions.[18–21] Building on these developments, here we demonstrate the use of bijels as soft matter templates for the synthesis of three-dimensional, co-continuous composite electrodes for electrochemical energy storage and conversion.

As seen in Fig. 1, our electrodes are comprised of three independently-percolating phases: (a) a nickel backbone, which serves as the current collector, (b) a thin coating of $Ni(OH)_2$ as the electrolytically active phase, and (c) an electrolyte solution of 6 M KOH that fills the remaining voids. $Ni(OH)_2$ chemistry was used here due to its relevance to electrochemical supercapacitors and batteries, low cost, relative safety, and well-known electrochemical characteristics. Further, previous theoretical and experimental studies with this chemistry provide a benchmark for comparison, allowing us to directly address the morphological benefits of bijel-derived materials for electrochemical applications. Our bijel-based composites offer the following unique microstructural attributes: (1) uniform pore geometry, (2) the ability to tune the internal surface area during bijel formation, and (3) the capability to independently adjust the active material thickness. Collectively, these control knobs enable microstructural tunability of the composite electrodes to simultaneously achieve a large volume fraction of active materials and rapid ion transport (short diffusion path) across the active phase, while maintaining co-continuous, low-resistance ion and electron transport paths throughout the entire structure. Finally, bijel-derived materials can be produced in bulk dimensions (several mm or larger overall sample size), as their initial formation is based on a spontaneous self-assembly process that produces uniform microstructural pattern throughout the entire mixture. Such characteristics are critical for engineering next generation electrochemical systems, and are not achievable in any of the previously reported techniques such as inverse opals, direct ink writing, foams, or lithography-based composites. With these unique morphological attributes, our method allows us to tune the salient electrochemical properties of our composites over a wide range and establish the bridge between supercapacitors and batteries with electrodes that simultaneously offer tunable, and large, power and energy densities.

Silica synthesis

Fluorescent silica particles with an average diameter of 697 nm and coefficient of variation of 2.6% were prepared *via* a modified Stöber process.[22,23] The dye was prepared by the addition of 12.5 mg of fluorescein isothiocyanate isomer (FITC) to a 20 mL vial containing 10 mL of anhydrous ethanol and 52.6 μL of 3-aminopropyltriethoxysilane and was stirred overnight. The silica particles were synthesized by the addition of 4.18 mL of tetraethylorthosilicate to a 250 mL flask containing 35 mL of anhydrous ethanol, 10 mL of ammonia, and 5 mL of the prepared dye solution, and allowing the reaction to proceed overnight. The particles were then washed in water by repeated centrifugation, dried in an oven at 70 °C for 4 hours, and then transferred to a vacuum oven maintained at 110 °C and allowed to dry for several days to obtain neutrally wetting properties.

Bijel formation and processing

Silica particles were dispersed in Millipore water *via* an ultrasonic probe at a power of 40 W for 4 minutes, and allowed to cool to room temperature. A known volume of 2,6-lutidine was then added to the silica dispersion to give a near-critical composition with respect to water ($x_{lut} = 0.064$). A vortex mixer was used to quickly agitate the sample, and 200 μL of the mixture was added to homemade microscopy vials (5 mm inner diameter cylindrical glass tubes). Bijels were then formed through exposure of the sample to microwave radiation at a power of 95 W for 30 seconds. Samples were transferred to an oven maintained at 70 °C and left unperturbed for 30 minutes.

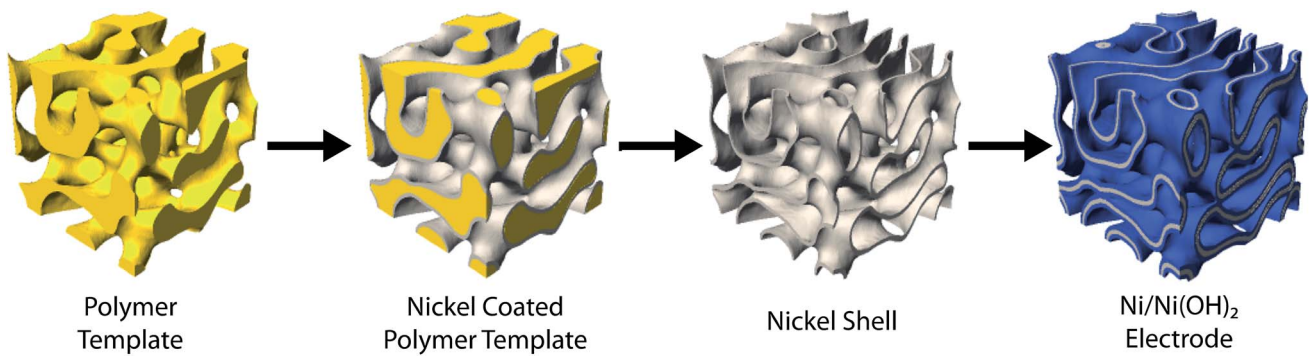

Fig. 1 Co-continuous bijel-based composite. Fabrication of a $Ni/Ni(OH)_2$ composite electrode from a bijel template.

Then, 70 μL of 1,6-hexandiol diacrylate monomer was carefully placed on top of the sample and allowed to diffuse into the lutidine-rich domains. After 5 hours, the liquid on top of the sample was removed and replaced with fresh monomer. After an additional 5 hours, keeping the samples above the critical temperature of 34.1 °C, photopolymerization was carried out using an ultraviolet lamp (Omnicure 1000, 40 W) for 80 seconds, producing a bicontinuous polymer sponge with bijel morphology. The silica particles were etched from the internal surfaces using 14.45 M hydrofluoric acid.

Nickel shell fabrication

The polymer template was immersed in a saturated solution of palladium chloride in anhydrous ethanol overnight. An electroless nickel-plating solution composed of 0.02 M nickel chloride hexahydrate, 0.02 M sodium tartrate dehydrate, and 1 M hydrazine was prepared. The pH of the plating bath was adjusted to 10 using sodium hydroxide and maintained at a temperature of 95 °C for the duration of the plating period (75 minutes). The sample was sintered in air at 300 °C for 4 hours and 500 °C for 4 hours to completely remove the polymer scaffold. The oxidized nickel sample was then reduced to nickel by sintering under 4% H_2 in Ar for 8 hours at 450 °C.

$Ni(OH)_2$ deposition

The $Ni/Ni(OH)_2$ composite was prepared by a known hydrothermal reaction.[16,24] Briefly, 32 mg of nickel chloride hexahydrate and 50 mg of urea were added to 20 mL of water, and transferred to an autoclave reactor along with the porous nickel scaffold. The reactor was heated to 180 °C for the desired time, and then allowed to cool down to room temperature. The resulting composite electrode was washed with deionized water and isopropyl alcohol, and allowed to dry overnight at 70 °C. The mass of the nickel hydroxide was carefully measured through weighing the sample before and after the deposition step using a Ragwag MYA 2.4 Y microbalance with 1 μg readability. Mass loading of $Ni(OH)_2$ for each electrode is given in Table S1.†

Characterization

Scanning electron microcopy was performed using a FEI Quanta 3D FEG Dual Beam microscope. All X-ray diffraction experiments were conducted using a Rigaku SmartLab. Electrochemical characterization and tests were done using a Solartron CellTest System Model 1470E controlled by CorrWare software.

Results and discussion

The $Ni/Ni(OH)_2$ composite electrodes were synthesized by simple chemical processing of bijel templates. Bijels were prepared by spinodal decomposition in a binary mixture of 2,6-lutidine and water, and arrested by interfacial jamming of colloidal silica particles 697 nm in diameter with a coefficient of variance of 2.6%.[16] The colloid volume fraction was varied from 0.014 to 0.040 to adjust the characteristic domain size, ξ. Bijels were transformed into bicontinuous polymer scaffolds by selectively polymerizing the lutidine phase with a hydrophobic monomer (1,6 hexanedioldiacrylate) mixed with a photoinitiator (Darocur 1173).[18] Nickel was then electrolessly deposited on the polymer scaffold to create a 1 μm thick coating on the outer surface of the polymer. The coated samples were sintered at 500 °C in air to completely remove the polymer, and subsequently sintered at 450 °C under H_2 (4% in Ar) to ensure the formation of pure nickel (Fig. S1a and b†). The resulting morphology, shown in Fig. 2a–c, is a highly porous nickel shell with uniform, continuous pores tuned in the range 8 μm < ξ < 22 μm. Utilizing other strategies, such as smaller particle size, even smaller domain sizes may be accessed. β-$Ni(OH)_2$ was deposited on the nickel shell by chemical bath deposition, creating the final composite electrode consisting of a conductive backbone coated with a thin layer of an electrolytically active material, and a continuous void phase. By controlling the deposition time, the active layer thickness, herein denoted as δ, was varied (δ = 475 nm, 675 nm, and 1 μm), as shown in Fig. 2d–f. Therefore, we created an array of electrodes with varying active material thicknesses and pore sizes, exemplifying the versatility in this fabrication technique. The electrodes will herein be referred to by their pore diameter in μm followed by the active coating thickness in nm, in the ξ/δ format (for example, 22/675 refers to the electrode with 22 μm pores and an active layer thickness of 675 nm).

Electrochemical characterization of the composites was performed using a three-electrode setup with a Pt wire counter electrode, Ag/AgCl reference electrode, and 6 M KOH electrolyte. As a representative example, cyclic voltammetry (CV) curves at varying scan rates for the 22/675 composite are shown in Fig. 3a. Each CV curve displays two clear peaks corresponding to the oxidation and reduction of the active material in the reversible reaction $Ni(OH)_2 \leftrightarrow NiOOH + H^+ + e^-$ and indicates that the capacity predominately originates from pseudo-capacitance rather than electronic double-layer capacitance.[25] A similar control experiment was performed on a bare nickel shell, and

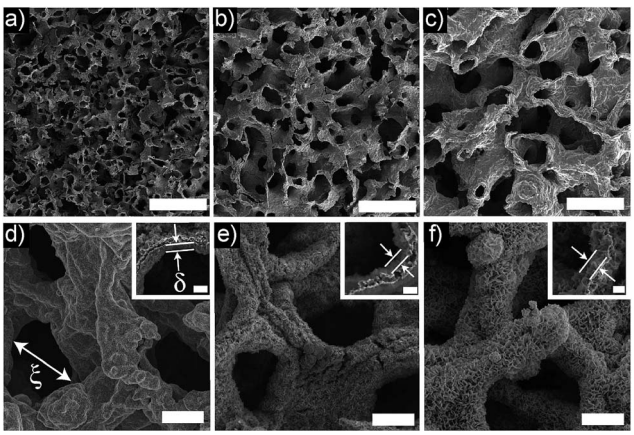

Fig. 2 Microstructure of the composite electrode. (a–c) Bare nickel shells with 8 μm, 15 μm and 22 μm domains. (d–f) The 15 μm electrode with three different active material thicknesses of 475 nm, 675 nm and 1 μm. The scale bars denote 25 μm for (a–c), 10 μm for (d–f), and 1 μm for the insets in (d–f).

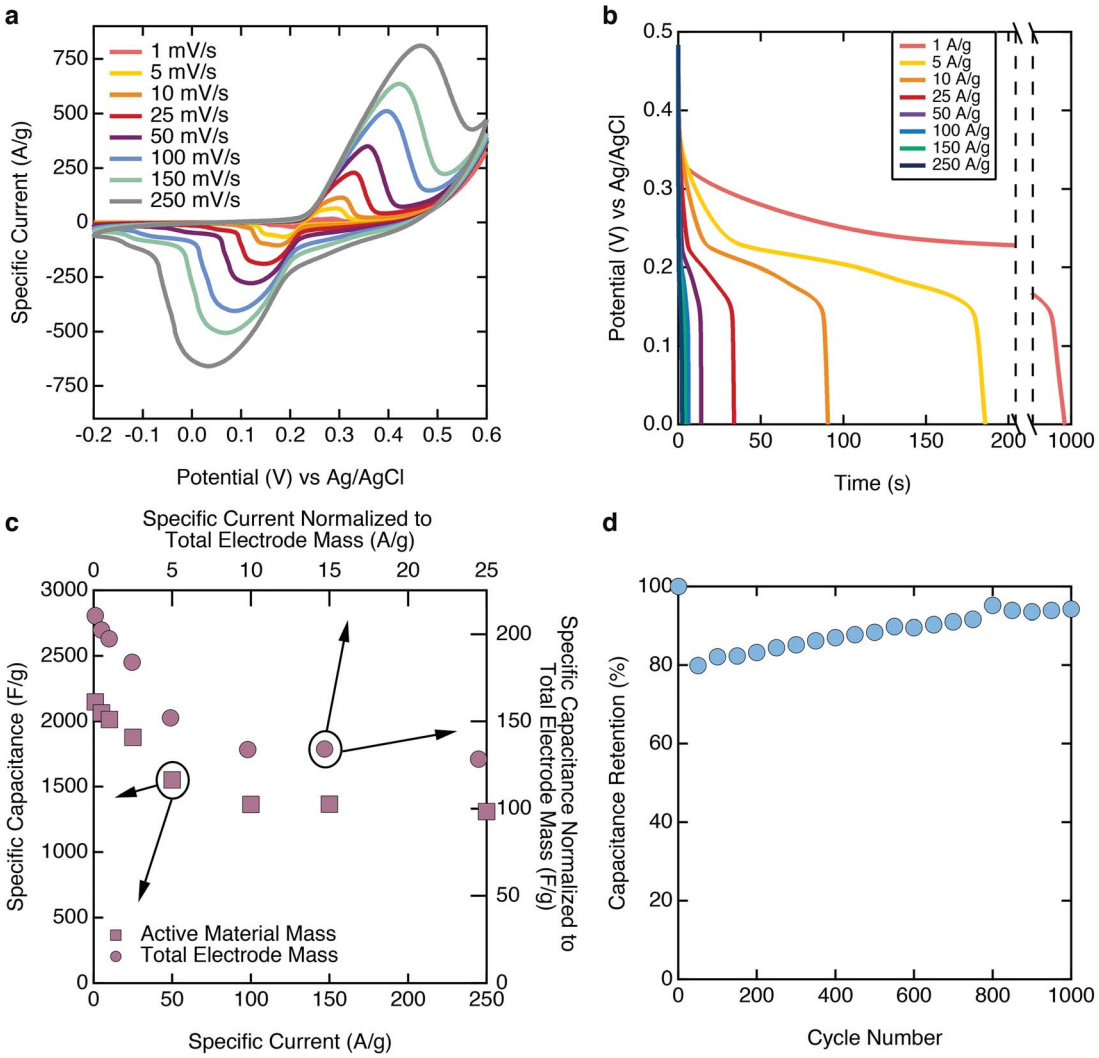

Fig. 3 Electrochemical characterizations of a representative Ni/$Ni(OH)_2$ electrode. (a) CV curves at various scan rates; (b) galvanostatic discharge curves at various current densities (c) gravimetric capacitance as a function of current density; (d) capacitance retention as a function of cycle number at a discharge rate of 25 A g^{-1}.

the resulting faradaic peaks were almost undetectable, confirming that the electrochemical performance predominantly originates from the electrolytically active material alone (ESI Fig. S2†). Clear redox peaks were still apparent at scan rates up to 250 mV s^{-1}, indicating the high-rate capability of this electrode. Specific capacitances were calculated from the discharge curves shown in Fig. 3b and a maximum gravimetric capacitance of 2148.5 F g^{-1} (based on the active material mass and the voltage window of 0.45 V used in the discharge tests) was achieved at a current density of 1 A g^{-1}, close to the theoretical value of 2305 F g^{-1}. Increasing the current density by an order of magnitude (from 1 to 10 A g^{-1}) decreased the gravimetric capacitance by only 6%, compared to a typical decrease of 30% or more in most of the published work on $Ni(OH)_2$ based electrodes.[24,26,27] Even at an outstanding current density of 250 A g^{-1}, the specific capacitance showed a decrease of only 39% (to 1310 F g^{-1}) from its maximum value, demonstrating the efficient use of active material in our bijel-based electrodes even at exceedingly large current densities. Taking into account the total mass of the electrode, a specific capacitance of 210.5 F g^{-1} was achieved at a current density 0.1 A g^{-1} (normalized to the total electrode mass), and increasing to 25 A g^{-1}, the electrode maintained a capacitance of 128.3 F g^{-1}. While the capacitance decreases significantly when considering the total mass of the electrode, which takes into account the mass of the inactive nickel backbone, it is still considerably higher than previously reported values for nickel foam based $Ni(OH)_2$ electrodes (12–38 F g^{-1})[8,28,29] and even modestly higher than some graphene foam based $Ni(OH)_2$ electrodes (166–183.1 F g^{-1}).[24,30] The corresponding CV and discharge curves for the other electrodes are presented in ESI Fig. S4–S9,† and show similar behavior as the 22/675 specimen. However, the 15/475 electrode exhibited a secondary reduction peak at high scan rates, which may be due to an ORR side reaction of the Pt mesh (see ESI Fig. S6 and S10†).[31] Therefore, our bijel-derived composites characteristically enable high current delivery with minimal loss in specific

capacitance, which stems from the unique way in which the active material is organized within the structure (in particular, its arrangement as a thin shell and accessibility throughout the volume due to the uniform pore morphology). To determine the long-term stability of our electrodes, the 22/675 specimen was tested at a current density of 25 A g^{-1} for 1000 cycles. As shown in Fig. 3d, the electrode demonstrated excellent stability, maintaining at least 80% of its original capacitance throughout the process. The initial drop in capacitance could be explained by poor wettability of the electrode in the electrolyte as well as a decrease in electrical contact between the current collector and active material.[32] The ensuing slow increase in capacitance could be caused by an activation process within the electrolytically active material that allows trapped ions to slowly diffuse out as well as an increasing improvement in the wettability of the electrodes surface by the electrolyte during subsequent cycles.[32] After 1000 cycles, the specific capacitance was maintained at 93% of its original value. Furthermore, SEM images of the sample revealed that its microstructure remained intact after the cycling test (ESI Fig. S11†), further corroborating the excellent mechanical stability of our electrodes.

As mentioned earlier, our method uniquely allows us to independently tune S_v (characterized here through variations in ξ) and δ during the bijel formation and chemical bath deposition steps, respectively. Together, these two morphological parameters govern the overall electrochemical performance of our system, since δ controls the length scale for ion transport into the active layer, and the product S_v. δ determines the volume fraction of active material. To demonstrate how independent control over these two parameters allows us to tune the electrochemical performance of our bijel-based electrodes, the gravimetric and volumetric energy and power densities of our materials are presented as Ragone plots in Fig. 4, and compared to other systems reported in the literature. The general shape of these graphs shows a roughly constant energy density until a critical power density is reached, which is presumably the point at which ion diffusion through the active layer begins to limit the electrode's performance. As seen in Fig. 4a, this critical specific power is correlated directly with δ, independent of the value of ξ. Therefore, discharge kinetics (and therefore power density) can be tuned in our systems through the active material thickness. In addition, each electrode reaches roughly the same specific energy (113.41 $\pm$ 3.4 W h kg^{-1} based on the mass of active material, 15.7 $\pm$ 4.32 W h kg^{-1} based on total electrode mass as shown in ESI Fig. S12†) at low specific power, indicating that our co-continuous design with uniform pore morphology enables usage of the entirety of the active material. The 15/475 electrode achieved the highest specific power (252 kW kg^{-1}) while preserving a modest specific energy (28.0 W h kg^{-1}, equivalent to 2.57 W h kg^{-1} at a specific power of 23.14 kW kg^{-1} when considering the total electrode mass). On a gravimetric basis, we exceed the best values reported in the literature, providing at least a 1.5× and up to a 10× improvement in energy density at comparable specific powers for all reported values.[24,26,32–34] This is again afforded by the unique architecture of our electrode, which allows for rapid energy delivery to and from the entirety of the active material, enabling battery-type specific energies and rate performances equivalent to or surpassing that of the best supercapacitors.

As discussed above, the superior specific power achieved in the 15/475 electrode is likely due to the small thickness of δ, providing a short diffusion path for ion transport through this layer. While this general strategy has already been employed in porous electrochemical composites by previous researchers, the

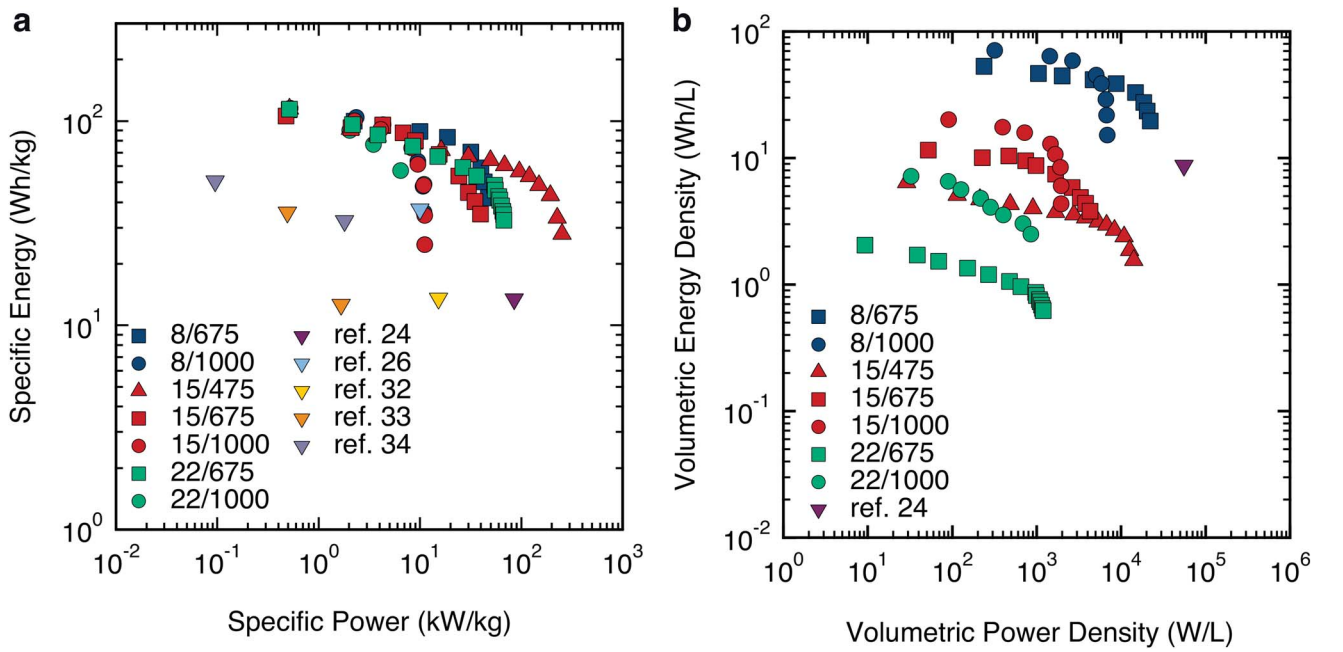

Fig. 4 Ragone plots. (a) Gravimetric and (b) volumetric energy and power densities of our bijel-based Ni/$Ni(OH)_2$ electrodes. For comparison, values for a number of other relevant systems (electrodes, full batteries and supercapacitors) from literature are also included.

entire electrode thickness has been purposely kept under 15 μm to ameliorate ion transport limitations into the tortuous pores, or due to constraints with the fabrication techniques implemented.[14,35] This approach then imposes a limit on the total amount of energy that can be stored in the cell. By contrast, the uniform, continuous pore morphology in our system provides minimal-resistance ion transport paths in the electrolyte phase, enabling specimens with thickness of at least ~500 μm, which is 30–50 times thicker than literature values for comparable systems.[13,14,24]

On a volumetric basis, accounting for the total volume of the half-cell (including the electrolyte in the pores), our electrodes show highly tunable performance, as presented in Fig. 4b. At low power densities, the volumetric energy density of our electrodes ranges from 2.047 to 70.88 W h L^{-1} as the volume fraction of active material is varied through S_v and δ. Further, our electrodes exhibit power densities up to 22.12 kW L^{-1} at high discharge rates, while still maintaining a large energy density of 19.66 W h L^{-1}. Fig. 4b compares our system with a state of the art $Ni(OH)_2$-based supercapacitor reported in literature, and shows that our electrodes can deliver similar energy and power densities.[24] However, it must be noted that the overall chemistries, while similar, are not exactly the same in these two systems. Further, our characterization was performed with a three-electrode setup, and to compare our results to previous studies in which a two-electrode setup or full cell were used, our measured energy densities were divided by a factor of four (see ESI†).[37] Therefore, comparisons between our electrodes and previous systems must be made with caution. Regardless, Fig. 4b directly demonstrates how the salient electrochemical properties of our composite electrodes can be tuned over a wide range by adjusting the two morphological parameters discussed above, which regulate the amount and spatial configuration of the active material in a given volume.

Collectivity, the gravimetric and volumetric Ragone plots in Fig. 4 underscore the exceptional tunability and performance of our co-continuous composites. To the best of our knowledge, this is the first system that facilely enables direct and independent tuning of the energy and power densities in these materials over a wide range to achieve power- and energy-dense electrodes through morphological adjustments at the length scales relevant to their electrochemical performance. As a result, our composites can outperform the best $Ni(OH)_2$ electrodes reported in the literature, due to a more efficient spatial arrangement of their various functional phases that is uniquely afforded in bijel-derived materials.

We postulated that the performance characteristics of our electrodes shown in Fig. 4 result from a kinetic competition between the cathode's electrochemical half-reaction and ion diffusion through the active layer. To test this hypothesis, we present a simple model for transient ion transport in a solid slab, in which the redox reaction at constant current density is represented by a zeroth-order term. Denoting the gravimetric power and energy densities as P and E respectively, the transient diffusion model has the solution (see ESI† for details):

$$E = \frac{nF\Delta V}{3.6L^2\rho}\sum_{i=0}^{\infty}\left[\frac{C_0}{{\lambda_i}^2} + \frac{2\rho P}{nF\Delta V D_H {\lambda_i}^4} \times \left(\exp\left(\frac{-{\lambda_i}^2 D_H C_0 nF\Delta V}{2\rho P}\right) - 1\right)\right], \quad (1)$$

where $n = 1$ is the stoichiometric number of electrons involved in the reaction, $F = 96\,485$ C mol^{-1} is Faraday's constant, ΔV is the applied voltage, L is the active layer thickness, ρ is the mass density of the active material, D_H is the mass diffusivity of protons through the active layer, C_0 is the initial concentration of oxidizing (OH) groups, and λ_i are the eigen values. To test the applicability of our model, we focus on the dominant ($i = 0$) terms in the series, for which the solution takes the form:

$$E = a_1 + a_2 P\left(\exp\left(-\frac{a_3}{P}\right) - 1\right), \quad (2)$$

with

$$a_1 = (nF\Delta V C_0)/(3.6L^2\rho{\lambda_0}^2),\ a_2 = 1/(1.8L^2 D_H {\lambda_0}^4),$$

and

$$a_3 = ({\lambda_0}^2 D_H C_0 nF\Delta V)/(2\rho).$$

Therefore, a three-parameter fit based on eqn (2) to the data in Fig. 4a would test the validity of the above model. It must be noted that the model parameters are not all freely adjustable: here the only unknowns are C_0 and D_H, for which theoretically expected values (or ranges) are available. As a representative example, Fig. 5a shows the data for the 8/675 electrode from Fig. 4a, together with a three-parameter fit based on eqn (2). Excellent agreement between the data and the model is observed, with $a_1 = 104.28$ W h g^{-1}, $a_2 = 1.1171$ s, and $a_3 = 32\,379$ kW kg^{-1}. A similar level of agreement is also achieved for the other specimens (see ESI†). From the collective values of the model parameters extracted from all experiments, we calculate $C_0 = 0.0485 \pm 0.0059$ mol OH^- per cm^3 and $D_H = 3.68 \times 10^{-9} \pm 2.93 \times 10^{-9}$ cm^2 s^{-1}, which are consistent with the theoretically expected $C_0 = 0.0885$ mol OH^- per cm^3 and 6.4×10^{-11} cm^2 s^{-1} $< D_H < 3.4 \times 10^{-8}$ cm^2 s^{-1} (ref. 36).

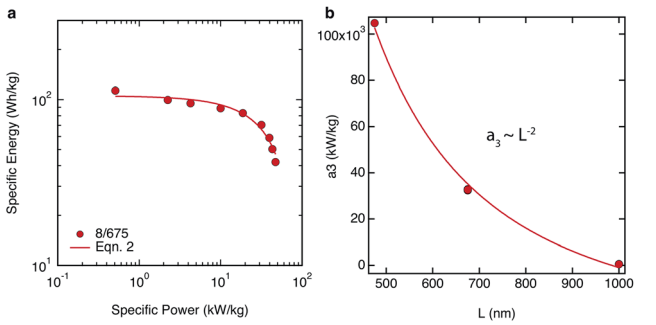

Fig. 5 Model predictions. (a) Data for the 8/675 electrode from Fig. 4a compared with the model predictions. (b) extracted a_3 values *versus* active material thickness compared to the expected L^{-2} dependency.

Our model also predicts that the critical power density, P_c, which is the value at which transport limitations begin to affect the electrode's performance, must scale with the active layer thickness as $P_c \sim nF\Delta VC_0D_H/2\rho L$.[2] From eqn (2), this occurs when P becomes comparable to a_3. Therefore, to further test the validity of our model, in Fig. 5b we compare the extracted values of a_3 for all electrodes (seven data points, some of which closely overlap with each other) with the predicted $1/L^2$ scaling. Again, our experimental observations are fully consistent with the predictions of our transient diffusion model. This analysis provides a mechanistic understanding of the electrode's performance as a kinetic competition between the redox reaction and ion transport within the active layer. In this context, any microstructural changes during charge/discharge will likely be manifested through variations in the diffusion coefficient.[37] The superior performance of our electrodes thus stems from our ability to simultaneously maintain a short ion diffusion path through the solid phase, a large volume fraction of the active material, high ion supply rates through the uniform electrolyte channels, and co-continuity of all phases. These characteristics, uniquely afforded by the particular morphology of our bijel-based composites, provide straightforward and rapid access to the entirety of the active material during the electrode's operation.

Conclusions

In conclusion, we have synthesized three-dimensional, co-continuous Ni/Ni(OH)$_2$ porous electrodes derived from bijels which offer robust tuning of the energy and power densities over a wide range, resulting in at least a 1.5× improvement in energy density over comparable systems previously reported in the literature. Further, our fabrication technique allows for electrodes that are significantly thicker than previously reported systems, enabling larger amounts of total stored energy. This level of performance is due to the unique microstructure of these bijel-derived composites, which are comprised of uniform, co-continuous phases whose characteristic length scales can be tuned independent of one another and within the range relevant to their electrochemical function. As such, electrodes can be designed to meet a variety of different performance characteristics. The synthesis strategy introduced here can be expanded beyond Ni/Ni(OH)$_2$ chemistries, offering a robust platform for the fabrication of microstructured composites for the next generation of electrochemical devices and energy materials.

Acknowledgements

Financial support for this work was provided by the National Science Foundation (CMMI 1301489) and the NASA Research Opportunities in Complex Fluids and Macromolecular Biophysics Program (NNX13AQ69G). J. A. W. acknowledges the U.S. Department of Education for a GAANN fellowship.

Notes and references

1 G. Wang, L. Zhang and J. Zhang, *Chem. Soc. Rev.*, 2012, **41**, 797–828.
2 J. Yan, Q. Wang, T. Wei and Z. Fan, *Adv. Energy Mater.*, 2014, **4**, 1300816.
3 J. R. Miller and P. Simon, *Science*, 2008, **321**, 651–652.
4 P. Simon and Y. Gogotsi, *Nat. Mater.*, 2008, **7**, 845–854.
5 J. W. Long, B. Dunn, D. R. Rolison and H. S. White, *Chem. Rev.*, 2004, **104**, 4463–4492.
6 D. R. Rolison, J. W. Long, J. C. Lytle, A. E. Fischer, C. P. Rhodes, T. M. McEvoy, M. E. Bourg and A. M. Lubers, *Chem. Soc. Rev.*, 2008, **38**, 226–252.
7 T. S. Arthur, D. J. Bates, N. Cirigliano, D. C. Johnson, P. Malati, J. M. Mosby, E. Perre, M. T. Rawls, A. L. Prieto and B. Dunn, *MRS Bull.*, 2011, **36**, 523–531.
8 G.-W. Yang, C.-L. Xu and H.-L. Li, *Chem. Commun.*, 2008, 6537–6539.
9 J. Zhu, Z. Gui, Y. Ding, Z. Wang, Y. Hu and M. Zou, *J. Phys. Chem. C*, 2007, **111**, 5622–5627.
10 J. Liu, C. Cheng, W. Zhou, H. Li and H. J. Fan, *Chem. Commun.*, 2011, **47**, 3436–3438.
11 H. Jiang, T. Zhao, C. Li and J. Ma, *J. Mater. Chem.*, 2011, **21**, 3818–3823.
12 X. Xiao, T. Beechem, D. R. Wheeler, D. B. Burckel and R. Polsky, *Nanoscale*, 2014, **6**, 2629–2633.
13 H. Zhang, X. Yu and P. V. Braun, *Nat. Nanotechnol.*, 2011, **6**, 277–281.
14 J. H. Pikul, H. G. Zhang, J. Cho, P. V. Braun and W. P. King, *Nat. Commun.*, 2013, **4**, 1732.
15 M. E. Cates and P. S. Clegg, *Soft Matter*, 2008, **4**, 2132–2138.
16 E. M. Herzig, K. A. White, A. Schofield, W. Poon and P. S. Clegg, *Nat. Mater.*, 2007, **6**, 966–971.
17 J. A. Witt, D. R. Mumm and A. Mohraz, *Soft Matter*, 2013, **9**, 6773–6780.
18 M. N. Lee and A. Mohraz, *Adv. Mater.*, 2010, **22**, 4836–4841.
19 M. N. Lee and A. Mohraz, *J. Am. Chem. Soc.*, 2011, **133**, 6945–6947.
20 M. N. Lee, J. H. Thijssen, J. A. Witt, P. S. Clegg and A. Mohraz, *Adv. Funct. Mater.*, 2013, **23**, 417–423.
21 M. N. Lee, M. A. Santiago-Cordoba, C. E. Hamilton, N. K. Subbaiyan, J. G. Duque and K. A. D. Obrey, *J. Phys. Chem. Lett.*, 2014, **5**, 809–812.
22 G. H. Bogush, M. A. Tracy and C. F. Zukoski, *J. Non-Cryst. Solids*, 1988, **104**, 95–106.
23 A. Van Blaaderen and A. Vrij, *Langmuir*, 1992, **8**, 2921–2931.
24 J. Ji, L. L. Zhang, H. Ji, Y. Li, X. Zhao, X. Bai, X. Fan, F. Zhang and R. S. Ruoff, *ACS Nano*, 2013, **7**, 6237–6243.
25 Z. Mao, P. DeVidts, R. E. White and J. Newman, *J. Electrochem. Soc.*, 1994, **141**, 54–64.
26 H. Wang, H. S. Casalongue, Y. Liang and H. Dai, *J. Am. Chem. Soc.*, 2010, **132**, 7472–7477.
27 L. L. Zhang, Z. Xiong and X. S. Zhao, *J. Power Sources*, 2013, **222**, 326–332.
28 X. Wang, Y. Wang, C. Zhao, Y. Zhao, B. Yan and W. Zheng, *New J. Chem.*, 2012, **36**, 1902–1906.

29 T. Xiao, X. Hu, B. Heng, X. Chen, W. Huang, W. Tao, H. Wang, Y. Tang, X. Tan and X. Huang, *J. Alloys Compd.*, 2013, **549**, 147–151.
30 J. Bai, B. Wang, L. Yu, L. Zhao, J. Wang, Q. Liu, J. Liu and Z. Li, *Electrochim. Acta*, 2015, **154**, 9–16.
31 W. Jin, H. Du, S. Zheng, H. Xu and Y. Zhang, *J. Phys. Chem.*, 2010, **114**, 6542–6548.
32 J. Yan, Z. Fan, W. Sun, G. Ning, T. Wei, Q. Zhang, R. Zhang, L. Zhi and F. Wei, *Adv. Funct. Mater.*, 2012, **22**, 2632–2641.
33 H. B. Li, M. H. Yu, F. X. Wang, P. Liu, Y. Liang, J. Xiao, C. X. Wang, Y. X. Tong and G. W. Yang, *Nat. Commun.*, 2013, **4**, 1894.
34 Z. Tang, C. Tang and H. Gong, *Adv. Funct. Mater.*, 2012, **22**, 1272–1278.
35 W. Liu, C. Ju, D. Jiang, L. Xu, H. Mao and K. Wang, *Electrochim. Acta*, 2014, **143**, 135–142.
36 S. Motupally, C. C. Streinz and J. W. Weidner, *J. Electrochem. Soc.*, 1998, **145**, 29–34.
37 M. Casas-Cabanas, J. Canales-Vázquez, J. Rodríguez-Carvajal and M. R. Palacín, *J. Am. Chem. Soc.*, 2007, **129**, 5840–5842.